Pis'ma v ZhETF, vol. 99, iss. 4, pp. 223 – 230 © 2014 February 25

Nitrogen-containing species in the structure of the synthesized nano-hydroxyapatite

M. Gafurov[1)], *T. Biktagirov, B. Yavkin, G. Mamin, Y. Filippov*[+], *E. Klimashina*[+], *V. Putlayev*[+], *S. Orlinskii*[1)]

Institute of Physics, Kazan Federal University, 420008 Kazan, Russia

[+]*Department of Materials Science, Lomonosov MSU, 119992 Moscow, Russia*

Submitted 9 January 2014

Synthesized by the wet chemical precipitation technique, hydroxyapatite (HAp) powders with the sizes of the crystallites of 20–50 nm and 1 μm were analyzed by different analytical methods. By means of electron paramagnetic resonance (EPR) it is shown that during the synthesis process nitrate anions from the reagents (by-products) could incorporate into the HAp structure. The relaxation times and EPR parameters of the stable axially symmetric NO_3^{2-} paramagnetic centres detected after X-ray irradiation are measured with high accuracy. Analyses of high-frequency (95 GHz) electron-nuclear double resonance spectra from ^{1}H and ^{31}P nuclei and *ab initio* density functional theory calculations allow suggesting that the paramagnetic centres and nitrate anions as the precursors of NO_3^{2-} radicals preferably occupy PO_4^{3-} site in the HAp structure.

DOI: 10.7868/S0370274X14040055

Introduction. Synthetic hydroxyapatite $Ca_{10}(PO_4)_6(OH)_2$ (HAp) is widely used for the variety of applications. Due to its excellent biocompatibility, osteoconductivity and chemical composition mirroring that of bone mineral and teeth enamel it is extensively employed for the hard tissues implantation. It is thought that HAp nanoparticles (nano-HAP) are better candidates for an apatite substitute of bone in biomedical applications than micro-sized hydroxyapatite (micro-HAp) [1]. Nano-HAp has the potential to improve current disease diagnosis due to their ability to circulate in the blood, to deliver and to distribute a payload to tissues and cells in the body for bioimaging and therapeutical applications [2]. High sorption activity to a number of various anions and cations makes the HAp based substances important not only in the biomedical area but also for waste management and in catalysts production [3–5]. High efficiency of HAp for the nitrate removal from the ground water was demonstrated in [6].

Conventional continuous-wave (cw) X-band (9 GHz) EPR (electron paramagnetic resonance) and ENDOR (electron-nuclear double resonance) methods are widely used for investigations of the radiation defects in apatite like materials. The obtained signals are usually ascribed to the different carbonate, phosphorous, hydroxyl, and oxygen radicals (see [7] for the recent review). Nitrogen-containg species though could be detected in the apatite-like materials [8–13] are not so extensively studied. It happens that their EPR spectra are not even recognized as due to the nitrogen [14, 15]. No nitrogen-containing centres were detected in the HAp of biogenic origin including bone or dental enamel [13, 16–18]. Though it is reported that low concentrations of the nitrogen-containing components in HAp used for implantation appear to be necessary for bone resorption, their high levels have an inhibitory effect [19]. A role of the nitrogen-containing impurities in HAp used for biomedical purposes is still debated. Localization of the N-containing inclusions in HAp is usually even not discussed. Methods of control of nitrogen compounds in small amounts in HAp (especially in nano-HAP) are not developed.

In this paper some capabilities and limitations of the commercial high-field/high frequency (HF EPR) of 95 GHz (W-band) and Fourier–Transform EPR spectrometers (FT-EPR) to study the nitrogen containing micro- and nano-HAp based materials in comparision to other analytical tools and "standart" EPR methods are shown. New experimental approaches to the identification, structure elucidation and localization of the nitrogen-containing species are presented. The experimental findings are supported by the density functional theory (DFT) calculations.

Materials and methods. *Synthesis of HAp powders.* For this work the nano-HAp powders with the stoichiometric formula $Ca_{10}(PO_4)_6(OH)_2$ were prepared by the wet preparation technique according to equation

[1)]e-mail: marat.gafurov@kpfu.ru; sergei.orlinskii@ksu.ru

$$10Ca(NO_3)_2 + 6(NH_4)_2HPO_4 + 8NH_4OH =$$
$$= Ca_{10}(PO_4)_6(OH)_2 + 20NH_4NO_3 + 6H_2O. \quad (1)$$

Briefly, 0.3 M stock solution of ammonium phosphate $(NH_4)_2HPO_4$ (3N purity, Labteh, Russia) was added in a drop-wise manner under constant stirring in an atmosphere of gaseous N_2 (to avoid carbonate contamination) to 0.5 M stock solution containing calcium nitrate ($(NO_3)_2 \cdot 4H_2O$) at desired ratio. The pH value of the stock solutions was pre-adjusted at 11.0(5) and then it was maintained manually at the constant value by addition of the concentrated solution of NH_4OH. After total mixing of the stock solutions, the suspension was ripened and heated to obtain micro- and nano-HAp: for 1 hour in one run (the case of 20 nm powder) up to 7 days for 1 μm powder under constant stirring and N_2-bubbling. Then, the precipitates were filtered, thoroughly washed with distilled water and allowed to dry at room temperature (RT) overnight. Other details are given in [5, 20].

Analytical methods. The samples were studied by X-ray diffraction (Cu Kα radiation, Rigaku D/MAX 2500) and FTIR spectroscopy in 400–4000 cm^{-1} range (Perkin–Elmer 1600). The micromorphology of the powders was examined by scanning and transmission electron microscopy (TEM, JEM-2000FX II, JEOL, operated at 200 kV and FESEM LEO SUPRA 50VP, Carl Zeiss, 5 kV). The Ca- and P-contents of the synthesized powders were extracted by energy dispersive X-ray fluorescence analysis (EDS, INCA Energy+, Oxford Instruments attached to LEO SUPRA 50VP). X-ray irradiation of the synthesized nanopowders was performed using URS-55 source ($U = 55$ kV, $I = 16$ mA, W – anticathode) at RT to create stable paramagnetic centres. FT (pulsed) and continuous wave EPR and ENDOR measurements were done by using X-band (9 GHz) and high-frequency (94 GHz, W-band) Bruker Elexsys 580/680 combined spectrometer.

EPR spectra were recorded by means of standart cw-technique as well as by means of field-swept two-pulse echo sequence (FS-ESE) $\pi/2 - \tau - \pi$ with the pulse length of π pulse of 16 (X-band) or 36 ns (W-band), correspondingly, and time delay $\tau = 240$ ns. For the phase-memory time measurements τ was varied from 200 ns up to the desired value with the minimal possible step of 4 ns. The Inversion–Recovery pulse sequence $\pi - \tau - \pi/2 - \tau - \pi$ for the spin-lattice relaxation times measurements was used. ENDOR spectra were detected by Mims sequence [7, 21] with the length of the radiofrequency (RF) pulse of 18 μs. Simulations of the obtained EPR spectra are done using EasySpin toolbox for MatLab [22].

Density functional theory based calculations. Ab-initio calculations were carried out within the plane-wave pseudopotential framework with the Perdew–Burke–Ernzerhof (PBE) [23] exchange-correlation functional. The Quantum ESPRESSO package [24] was used. Unit-cell and initial positional parameters for HAp were taken from [25]. The $1 \times 2 \times 1$ monoclinic supercell (space group $P2_1/b$; 176 atoms in case of pure HAp) was used for the calculations. To analize possible influences of the supercell size on the calculated properties 44- and 88-atoms configuration were also considered. Preliminary structural optimization together with the analysis of the total energies was performed using Vanderbilt ultrasoft pseudopotentials [26] with kinetic energy cutoffs of 40 Ry for the smooth part of the electron wave functions and 320 Ry for the augmented electron density (as defined by the convergence test). Parameters of the hyperfine interaction of the unpaired electron with ^{14}N and ^{1}H nuclei were extracted by using the gauge–including projector augmented wave (GIPAW) approach [27] with Troullier–Martins pseudopotentials [28] and the plane-wave energy cutoff of 60 Ry. The Brillouin Zone integration was restricted to Γ-point during structural optimization, whereas the Monkhorst–Pack [29] k-point mesh with the reciprocal spacing of about 0.35 nm^{-1} in each lattice direction was used for the calculation of the constants of hyperfine interaction.

Results. The synthesized according to Eq. (1) nanopowders of $Ca_{10}(PO_4)_6(OH)_2$ are EPR silent. No traces of the nitrogen containing impurities are determined neither by EDS (with the beam energy below 10 keV) nor by FTIR spectroscopy.

XRD analysis show that all the samples contain only one phase corresponding to the space group $P6_3/m$ with the parameters of the unit cell close to $a \approx b \approx 0.942$ nm and $c \approx 0.688$ nm typical for the bulk crystals of the hydroxyapatite [3]. Sizes of crystallites were estimated from the diffraction line profile (002) [30]. Corresponding EDS investigations ensure the ratio Ca/P = 1.66(2). XRD patterns before and after X-ray irradiation with the doses of 5 and 10 kGy are measured to be the same.

The EPR spectrum of X-ray irradiated nano-HAp samples with an average size of 30 nm recorded in cw-mode at RT is presented in Fig. 1a. After X-ray irradiation with the doses of 5, 10, and 100 kGy the amplitude of the EPR signal remains the same. Induced radicals' concentration of $5(1) \cdot 10^{18}$ spins per gram was estimated from the comparison of the integrated intensity of the spectra with that from the standart reference sample (Mn^{2+} in MgO).

Fig. 1b presents the EPR spectrum obtained by FS-ESE in X-band ($\nu = 9.6$ GHz) at RT along with the

Table 1

EPR parameters extracted from the simulations of the RT FS-ESE *X*-band spectra (Fig. 1b)

Modification	$g_\parallel$	$g_\perp$	$A_\parallel$, mT	$A_\perp$, mT	Statistical weight
MI	2.0011(1)	2.0052(1)	6.65(40)	3.37(5)	>66 %
MII	2.0011(1)	2.0052(1)	6.65(40)	3.64(5)	<17 %
MIII	2.0011(1)	2.0052(1)	6.65(40)	3.05 (10)	<17 %

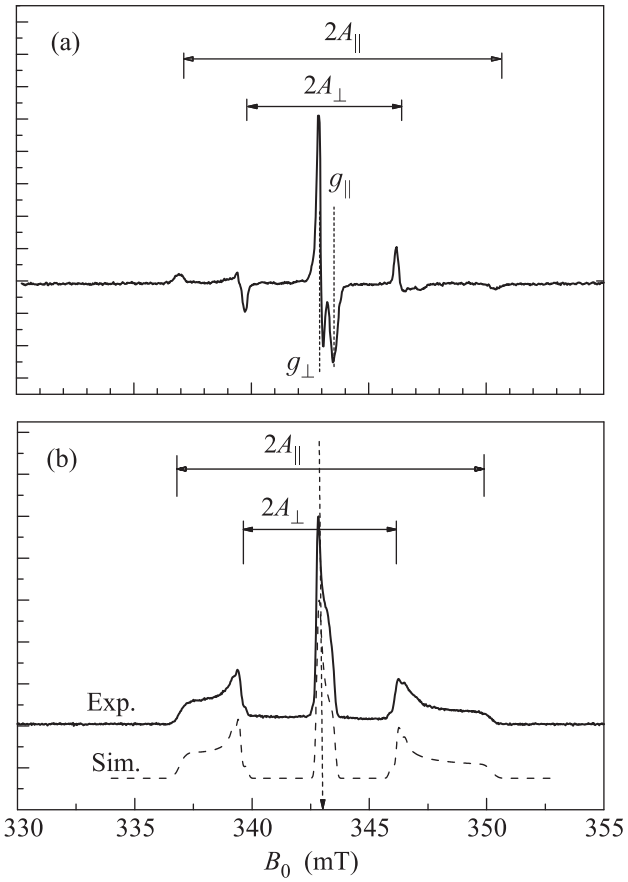

Fig. 1. EPR spectra in a powder of $Ca_{10}(PO_4)_6(OH)_2$ nanoparticles (30 nm) after X-ray irradiation in X-band at $T = 298$ K measured in cw-mode (a) and in FS-ESE mode (b) (exp) along with the simulation for NO_3^{2-} radical curve (sim) with the parameters given in Table 1. Simulation curve is vertically shifted for convenience. The vertical dashed arrow points the value of B_0 in which ENDOR spectra are acquired and relaxation times are measured

simulation for NO_3^{2-} type radical (see next section for details). It gives an opportunity to measure the characteristic relaxation times of the centres observed. For X-band at $T = 298$ K spin-lattice (longitudinal) relaxation time $T_{1e} = 22(2)\,\mu$s is estimated from the inversion-recovery experiments while the phase-memory (transversal) time $T_2* = 5.3(2)\,\mu$s from the spin-echo decay in the magnetic field B_0 corresponding to the perpendicular orientation of the nanocrystals investigated (vertical dashed arrow in Fig. 1b).

In [16] it was proposed that the HAp components of the aorta organomineralic matrix could serve at least as markers for the diagnosis of the atherosclerotic plaque formation/rupture risks. Advantages of the increased resolution and sensitivity of the HF EPR methods were applied to detect and quantify the tissues containing the carbonate radicals in nano-HAp inclusions for the early diagnosis [16], to investigate spectral and relaxation characteristics of the naturally existing manganese or intentionally incorporated lead ions and to establish their locations in atherosclerotic plaque and nano-HAp structures [17, 18, 31]. W-band FS-ESE detected EPR spectrum of the 20 nm sample at $T = 50$ K is presented in Fig. 2. Relaxation times $T_{1e} = 30(1)\,\mu$s and

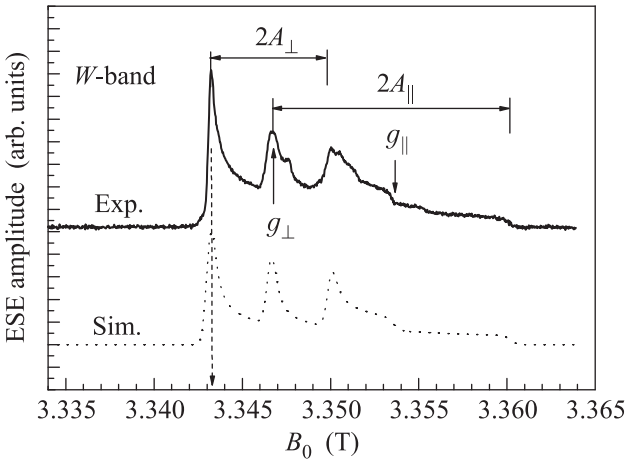

Fig. 2. FS-ESE EPR spectrum obtained in a powder of nano-HAp (20 nm) after X-ray irradiation in the W-band, 50 K (exp). Simulation curve (sim) for the NO_3^{2-} radical with the same parameters as for the X-band measurements (Table 1) is vertically shifted for convenience. The vertical dashed arrow marks the value of B_0 in which the relaxation times and ENDOR spectra are measured

$T_2* = 8.3(3)\,\mu$s are estimated at $T = 300$ K in the magnetic field B_0 corresponding to the maximal obtained ESE (dashed arrow on Fig. 2). Nature of the additional

splittings detected in the W-band experiments due to the increased spectral resolution and sensitivity of the HF EPR, we ascribe to the presence of carbonate radicals [16] and to some paramagnetic centre(s) with the spectroscopic g-factor close to that of the free electron.

To specify the coordination of the obtained paramagnetic centres ENDOR experiments were carried out. Fig. 3 presents the Mims-ENDOR spectra in the vicinity of phosphorous (^{31}P) and hydrogen (^{1}H) Larmor frequencies obtained in W-band at $T = 50$ K.

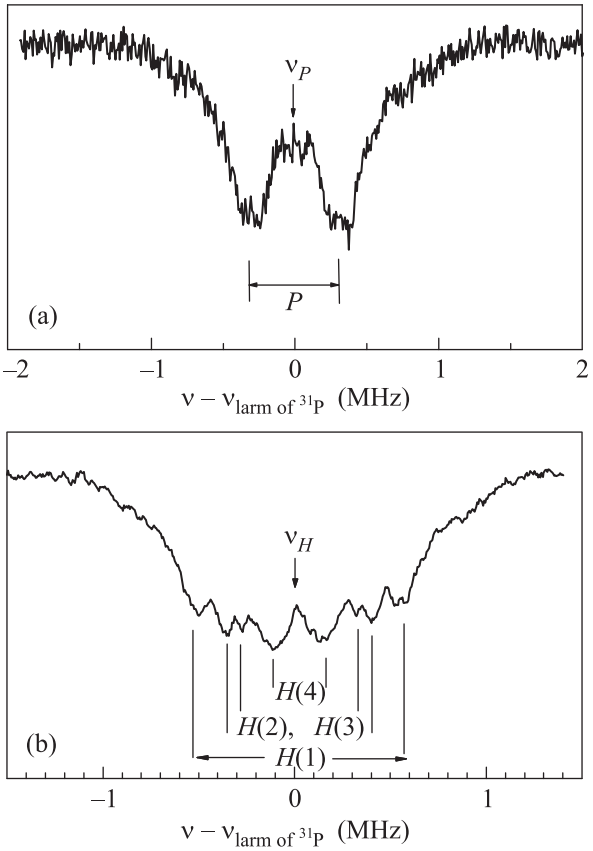

Fig. 3. ENDOR spectra of the X-ray irradiated nano-HAp in the vicinity of (a) phosphorous and (b) hydrogen Larmor frequencies; W-band, 50 K

No significant difference between the EPR and ENDOR signals or relaxation times were observed with the size of the powder grains that is typcal for the localized paramagnetic centres. No changes of the observed EPR, ENDOR signals or relaxation times were monitored even after samples annealing up to 400 °C for 4 hours under vacuum ($< 10^{-4}$ mbar). Our attempts to replace the observed paramagnetic centres by washing the HAp powders before and after X-ray irradition in a NaOH or HCl solutions in a wide pH range (3–12) also do not reveal a significant change in EPR or ENDOR spectra or relaxation characteristics. All these demonstrate that the observed radicals are not located on the powder grain surface but most probably are incorporated into the HAp structure of the investigated HAp nanopowders.

Discussion. *EPR spectra.* The position of the EPR spectra and observation of the three-line pattern with the characteristic splitting for crystals (due to the hyperfine interaction between the electronic spin with $S = 1/2$ and one nuclear spin with $I = 1$) can be ascribed to the presence of stable nitrogen-containing paramagnetic centre (for ^{14}N isotope with the natural abundance of 99.6 %, $I = 1$). The observed X-band spectra (Fig. 1) present typical powder spectra that can be described by the spin-Hamiltonian of the axial symmetry

$$H = g_{\parallel}\beta B_z S_z + g_{\perp}\beta(B_x S_x + B_y S_y) + \\ + A_{\parallel} S_z I_z + A_{\perp}(S_x I_x + S_y I_y), \qquad (2)$$

where $g_{\parallel}$ and $g_{\perp}$ are the main components of the g-tensor, $A_{\parallel}$ and $A_{\perp}$ are the main components of the hyperfine tensor, B_i, S_i, and I_i are the projections of the external magnetic field strength, electronic spin $S = 1/2$ and nuclear spin $I = 1$, correspondingly, onto the $i = x, y, z$ coordinate axis, β is a Bohr magneton.

The values listed in Table 1 are derived from the simulations of the ESE spectrum (Fig. 1b). They show the presence of at least three paramagnetic centres of the same origin (denoted as M for "modification"). In simulations it is assumed that A- and g-tensors are coliniear.

The X-band spectra could be simulated nicely if we suppose a Gaussian (continuous) distribution of $A_{\parallel}$ with a deviation of 0.40 mT around the mean value of 6.65 mT and discrete distribution of $A_{\perp}$ around 3.37 mT while the components of g-factors for all of the obtained radical's modifications are the same. The most intensive signal from the modification denoted as MI is overlapped by two others in less concentrations (Table 1). Different stable inorganic radicals trapped in natural and synthesized crystals could be detected and separated by EPR. A number of the EPR experiments supported by theoretical calculations show that generally the most RO_2 type radicals (like NO_2, NO_2^{2-}) have anisotropic hyperfine interaction and g-tensors with all three principal values unequal. The RO_3 type radicals (NO_3, NO_3^{2-}), on the other hand, have an axially symmetric hyperfine interaction tensor and (in the most cases) g-factor [7–12, 33–36]. It could be expected also that due to the additional rotational mobility of RO_2 and OROO type radicals along O–R–O axis [36, 37] their electronic spin-lattice relaxation times should be

shorter than those for RO_3 and it might be problematic to obtain ESE detected EPR of those in HAp at RT. Based on the values of g- and A-tensors obtained in our experiments we can conclude that the X-band and W-band EPR spectra are undoubtedly due to the presence of NO_3^{2-} type radical.

In addition to [9, 11, 12] we have managed to detect one more NO_3^{2-} (MIII) modification with even smaller value of $A_\perp$ in X-ray irradiated material and did not observe great changes in the EPR spectra after annealing up to 400 °C in our nano-HAp samples. It seems to be that the variety of the modifications obtained in HAp is caused by the quality of the samples rather than by the type of the radiation source and its dose. No detailed theoretical study of NO_3^{2-} is known.

As mentioned, some researchers still incorrectly interpret the similar to Fig. 1a EPR spectrum ascribing it to other types of radicals [14, 15]. This fallacy is caused among other things by the absence of the nitrate bands in the vicinity of 825 and 1385 cm^{-1} in IR patterns of HAp [38, 39]. The lack of the nitrate infrared response could be ascribed to the low nitrate concentration, IR lines broadening with the particle size decrease or to their overlap with the intensive, broad PO_4^{3-} bands. In this sense the exploited EPR routines could serve as a sensitive supplement to the recognized methods of the nitrate detection [40].

Authors of [14] have attributed the same cw-EPR spectrum as we obtained (see Fig. 1a) to the HCO type radical. But it is not our case: the intensity (amplitude) of the discussed EPR signal in the carbonated samples prepared with the same procedure as described (see [39]) goes down with the carbonation level and becomes negligible at the carbonate concentrations of 8 wt. %.

ENDOR spectra. Superhyperfine interaction, characterized by the superhyperfine constant a, between the electron cloud of NO_3^{2-} radical and neighbouring nuclei with $I = 1/2$ and 100 % abundance like ^{31}P and ^{1}H leads to the splitting of the ENDOR spectra according to

$$\nu_{\mathrm{ENDOR}} = h^{-1}|g^{(I)}\beta^{(I)}B_0 \pm a/2|, \qquad (3)$$

where h is a Planck constant, $g^{(I)}$ is a nuclear g-factor and $\beta^{(I)}$ is a nuclear Bohr magneton [7, 21]. For the first approximation, assuming the pure electron-nuclei dipole-dipole interaction in the point model, the electron-nuclear distances, r, from the ENDOR splitting can be estimated as:

$$a \propto g \cdot g^{(I)}(1 - 3\cos^2\Theta)/r^3, \qquad (4)$$

where Θ is an angle between the directions of $g_\parallel$ and B_0. Spectral resolution of the W-band experiments allows to choose the value of B_0 corresponding to the "pure" perpendicular orientation $g_\perp$. In this case the factor $1 - 3\cos^2\Theta = 1$. The calculations are registered as r_{exp} in Table 2. One phosphorous and different hydrogen nuclei neighbouring the radical could be distinguished (see Fig. 3). Due to the closeness of the spectroscopic parameters of all three modifications MI–MIII to each other (cf. Table 1), it is expected that all of them give an equal contribution to the ENDOR spectrum.

Assuming that the unpared electron is mostly localized on N, we have compared the distances between the all possible atomic positions that can be N-substituted and the nearest hydrogen and phosphourous atoms with our ENDOR results. Such "screening" allowed us to choose two crystallographic sites for the nitrogen atom of the nitrate ion: N(1) that substitutes two close hydrogen sites in OH-channel and N(2) that substitutes O atom of the phosphate tetrahedron of HAp structure. The distances between these positions and the nearest hydrogen and phosphorous atoms (r_{calc}), derived from the undistorted perfect HAp crystal structure [3] are listed in Table 2. The positions N(1) and N(2) appear to be the most probable for the nitrate incorporation (as in the case of carbonate substitution they can be designated as A- and B-sites, respectively).

DFT calculations. To define a structure and location of NO_3^- ion, we have considered two possible models of its incorporation as suggested by ENDOR. For the N(2) site a charge compensation is required. As it is usually assumed for the carbonate-doped HAp, we suggest that the charge compensation scheme is manifested in the removal of one of the nearest Ca [41]. We have performed full geometry optimization runs with different initial configurations in order to be sure that the energetically most favorable structures are obtained.

As it follows from the computations, for both of the defect models the substitutional nitrate ion has almost identical planar configuration with the average N–O distance of about 0.126 nm. The lattice parameters for both of the simulated models are appearing to be very close to those for pure HAp (the deviations do not exceed 1 % from the obtained experimentally). We found no effect of the supercell size on the calculated properties.

In order to study the structure and magnetic properties of the paramagnetic NO_3^{2-} centre we have performed spin-polarized calculations with one extra electron added to supercell. The structural relaxation was carried out with respect to atomic positions with the lattice parameters fixed. The optimized supercells containing NO_3^- impurity were used as initial data. The structure of the resulting NO_3^{2-} radical shows significant deviation from the planarity for both B- and A-sites towards to the pyramidal shape. The out of plane

Table 2

ENDOR splittings, electron-nuclear distances extracted from the ENDOR experiments using Eq. (4) in the point-point dipole-dipole interaction approach (r_{exp}), distances between the atom in substituted OH and PO_4^{3-} positions and the nearest ^{1}H and ^{31}P nuclei extracted from the crystal structure of perfect HAp [3], and from the DFT optimized impurity containing structures (r_{calc}) and total deviation between r_{exp} and r_{calc}

Nucleus	ENDOR splitting (MHz)			r_{exp} from W-band 50 K nm	r_{calc} from the indicated positions to the nearest nuclei in the HAp structure, nm			
	X-band, RT	W-band, RT	W-band, 50 K		OH channel, position N(1)	PO_4^{3-} position, N(2)	OH channel position, DFT	PO_4^{3-} position, DFT
H(1)	0.66(20)	0.78(12)	1.06(1)	0.42(1)	0.32	0.48	0.3	0.42
H(2)	–	–	0.75(1)	0.47(1)	0.37	0.5	0.42	0.47
H(3)	–	–	0.60(1)	0.51(1)	0.66	0.67	0.64	0.57
H(4)	–	–	0.26(1)	0.67(1)	0.71	0.71	0.74	0.61
P	0.72(25)	0.70(20)	0.64 (6)	0.37(1)	0.40	0.32	0.36	0.4
–	–	–	–	$\Sigma(r_{exp}-r_{calc})^2$	0.045 nm^2	0.034 nm^2	0.039 nm^2	0.008 nm^2

deviation is estimated to be of about 13°. The values of the spin density localization on ^{14}N are found to be of 0.3 e/bohr^3 for the A-site and 0.37 e/bohr^3 for the B-site. The principal values of the ^{14}N hyperfine tensor obtained using GIPAW method are presented in Table 3. We note that the calculated parameters do not

Table 3

GIPAW DFT calculated ^{14}N hyperfine components for the A-type (OH channel) and B-type (PO_4^{3-} site) of substitution (in mT)

Position	A_{xx}	A_{yy}	A_{zz}
A-site, N(1)	2.49	2.48	5.18
B-site, N(2)	3.28	3.27	6.41

depend significantly on the supercell size. From the excellent correspondence with the experimental results (cf. Table 1), it can be concluded that the obtained EPR spectra originate from the B-site located radicals only.

We have recovered the interatomic distances from the relaxed NO_3^{2-} containing HAp supercells (see Table 2). The good agreement with the distances derived from ENDOR data justifies the B-type location of the impurity. We have simulated the partial contributions to ENDOR spectrum due to the protons located near to the impurity site by using ^{1}H hyperfine tensors as followed from GIPAW DFT calulations. The simulated ^{1}H ENDOR spectra together with the optimized structure of the NO_3^{2-} radical in the B-position of HAp are illustrated on Fig. 4. Only the contributions due to the three nearest protons (with N–H interatomic distances within 0.6 nm) are shown; the other protons contribute only to the region close to the Larmor frequency.

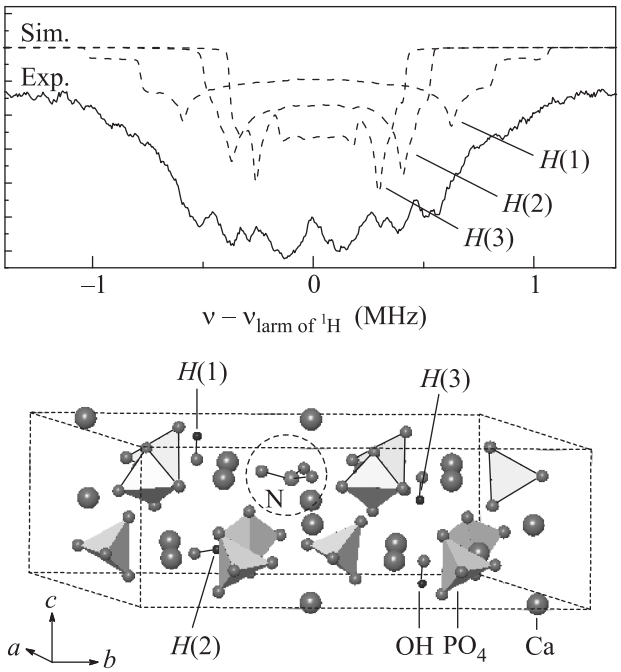

Fig. 4. Top – ENDOR spectra simulated separately for the protons nearest to the defect site as followed from the GIPAW DFT calculations (dashed) presented together with the experimental ^{1}H ENDOR spectrum (solid). Bottom – optimized structure of the stable NO_3^{2-} radical in B-position (N(2) site) of HAp (the tetrahedra are for PO_4 groups); the protons taken into account in ENDOR simulation are marked

Conclusion and perspectives. Modern EPR approaches can complement standard analytical tools for the comprehensive characterization of the HAp based materials [43–45] and could be used for the quality check, estimations of the crystallinity and purity of the

synthesized species and for the further structural investigations of nano-HAP.

NO_3^{2-} radicals with slightly different spectroscopic parameters in the wet-synthesized HAp samples are detected by FT-EPR. According to the perfomed DFT calculations, they all are due to the *B*-type located radicals. The variation of the spectroscopic parameters might be due the slightly different geometry of the radical or to the re-distribution of the nearest vacancies. No powder grain size effects was found in our experiments.

We hope that the presented work could serve as an another node for the detailed investigation of different nanostructures and stimulate the scientific community for their study by other advanced magnetic resonance techniques. All these, finally, could help to synthesize the materials with the increased biocompatibility and higher efficiency for the removal of different toxic elements.

The authors Y.F., E.K., and V.P. acknowledge partial support from Lomonosov Moscow State University Program of Development, Russian Foundation for Basic Research under Grants # 12-03-01025, 12-08-00681, 12-08-33125, 13-08-12236, and 13-08-01056. T.B. acknowledges the possibility to use some computational abilities of Institute of Physics of Kazan Federal University for DFT.

1. H. Zhou and J. Lee, Acta Biomater **7**, 2769 (2011).
2. S. C. J. Loo, T. Moore, B. Banik, and F. Alexis, Curr. Pharm. Biotechnol. **11**, 333 (2010).
3. J. C. Elliott, Stud. Inorg. Chem. **18**, 1 (1994).
4. *Modern heterogeneous oxidation catalysis: design, reactions and characterization*, ed. by N. Mizuno, Weinheim, Wiley–VCH (2009).
5. B. V. Yavkin, G. V. Mamin, S. B. Orlinskii, M. R.Gafurov, M. Kh. Salakhov, T. B. Biktagirov, E. S.Klimashina, V. I. Putlyaev, Yu. D. Tretyakov, and N. I. Silkin, Phys. Chem. Chem. Phys. **14**, 2246 (2012).
6. M. Islam, P. C. Mishra, and R. Patel, J. Environ Manage **91**, 1883 (2010).
7. P. Fattibene and F. Callens, Appl. Rad. Isot. **68**, 2033 (2010).
8. R. S. Eachus and M. C. R. Symons, J. Chem. Soc. A 790 (1968).
9. V. V. Nosenko, I. P. Vorona, S. S. Ishchenko, N. P.Baran, I. V. Zatovsky, N. A. Gorodilova, and V. Yu. Povarchuk, Radiat Meas. **47**, 970 (2012).
10. T. Murata, K. Shiraishi, Y. Ebina, and T. Miki, Appl. Rad. Isot. **47**, 1527 (1996).
11. I. P. Vorona, S. S. Ishchenko, N. P. Baran, V. V. Rud'ko, I. V. Zatovskii, N. A. Gorodilova, and V. Yu. Povarchuk, Phys. Solid State **52**, 2364 (2010) [Fizika Tverdogo Tela **52**, 2364 (2010)].
12. N. P. Baran, I. P. Vorona, S. S. Ishchenko, V. V. Nosenko, I. V. Zatovskii, N. A. Gorodilova, and V. Yu. Povarchuk, Phys. Solid State **53**, 1891 (2011) [Fizika Tverdogo Tela **53**, 1891 (2011)].
13. A. B. Brik, A. P. Shpak, A. P. Klimenko, V. L. Karbovskaya, V. A. Oak, A. M. Kalinichenko, N. N. Bagmut, and V. V. Bevz, Miner. J. (Ukraine) **28**, 20 (2006).
14. D. Schramm and A. Rossi, Phys. Chem. Chem. Phys **1**, 2007 (1999).
15. D. V. Rokhmistrov, O. T. Nikolov, O. A. Gorobchenko, and K. I. Loza, Appl. Rad. Isot. **70**, 2621 (2012).
16. V. A. Abdul'yanov, L. F. Galiullina, A. S. Galyavich, V. G. Izotov, G. V. Mamin, S. B. Orlinskii, A. A. Rodionov, M. Kh. Salakhov, N. I. Silkin, L. M. Sitdikova, R. N. Khairullin, and Y. A. Chelyshev, JETP Lett **88**, 69 (2008) [Pis'ma v ZhETF **88**, 75 (2008)].
17. M. R. Gafurov, B. V. Yavkin, T. B. Biktagirov, G. V. Mamin, S. B. Orlinskii, V. V. Izotov, M. Kh. Salakhov, E. S. Klimashina, V. I. Putlayev, V. A. Abdul'yanov, I. M. Ignatjev, R. N. Khairullin, A. V. Zamochkin, and Yu. A. Chelyshev, Magn. Reson Solids **15**, 13102 (2013).
18. T. B. Biktagirov, Y. A. Chelyshev, M. R. Gafurov, G. V. Mamin, S. B. Orlinskii, Y. N. Osin, and M. Kh. Salakhov, J. Phys.: Conf. Ser. **478**, 012002 (2013).
19. M. V. J. Hukkanen, J. M. Polak, and S. P. F. Hughes, *Nitric oxide in bone and joint disease*, Cambridge, Cambridge University Press (1998).
20. E. S. Kovaleva, M. P. Shabanov, V. I. Putlyaev, Y. D. Tretyakov, V. K. Ivanov, and N. I. Silkin, Cent. Eur. J. Chem. **7**, 168 (2009).
21. D. M. Murphy and R. D. Farley, Chem. Soc. Rev. **35**, 249 (2006).
22. S. Stoll and A. Schweiger, J. Magn. Reson. **178**, 42 (2006).
23. J. P. Perdew, K. Burke, and M. Ernzerhof, Phys. Rev. Lett. **77**, 3865 (1996).
24. P. Giannozzi, S. Baroni, N. Bonini, M. Calandra, R. Car, C. Cavazzoni, D. Ceresoli, G. L. Chiarotti, M. Cococcioni, I. Dabo, A. Dal Corso, S. Fabris, G. Fratesi, S. de Gironcoli, R. Gebauer, U. Gerstmann, C. Gougoussis, A. Kokalj, M. Lazzeri, L. Martin-Samos, N. Marzari, F. Mauri, R. Mazzarello, S. Paolini, A. Pasquarello, L. Paulatto, C. Sbraccia, S. Scandolo, G. Sclauzero, A. P. Seitsonen, A. Smogunov, P. Umari, and R. M. Wentzcovitch, J. Phys Condens Matter **21** , 395502 (2009).
25. M. Yashima, Y. Yonehara, and H. Fujimori, J. Phys. Chem. C **115**, 25077 (2011).
26. D. Vanderbilt, Phys. Rev. B **41**, 7892 (1990).
27. C. J. Pickard and F. Mauri, Phys. Rev. B **63**, 245101 (2001).
28. N. Troullier and J. L. Martins, Phys. Rev. B **43**, 1993 (1991).
29. H. J. Monkhorst and J. D. Pack, Phys. Rev. B **13**, 5188 (1976).

30. T. H. De Keijser, J. I. Langford, E. J. Mittemeijer, and A. B. P. Vogels, J. Appl. Cryst. **15**, 308 (1982).
31. B. V. Yavkin, M. R. Gafurov, S. S. Kharintsev, G. V. Mamin, E. Goovaerts, M. Kh. Salakhov, Y. N. Osin, and S. B. Orlinskii, J. Phys.: Conf. Ser. **478**, 012001 (2013).
32. J. R. Morton, Chem. Rev. **64**, 453 (1964).
33. R. P. Wayne, I. Barnes, P. Biggs, J. P. Burrows, C. E. Canosa-Mas, J. Hjorth, G. Le Bras, G. K. Moortgat, D. Perner, G. Poulet, G. Restelli, and H. Sidebottom, Atmos Environ A **25**, 1 (1991).
34. J. F. Stanton, J. Chem. Phys. **126**, 134309 (2007).
35. S. I. Bannov, V. A. Nevostruev, Rad. Phys. Chem. **68**, 917 (2003).
36. J. Dugas, B. Bejjaji, D. Sayah, and J. C. Trombe, J. Sol. State Chem. **24**, 143 (1978) (in French).
37. T. M. Pietrzak and D. E. Wood, J. Chem. Phys. **53**, 2454 (1970).
38. M. Palard, E. Champion, and S. Foucaud, J. Sol. State Chem. **181**, 1950 (2008).
39. E. S. Kovaleva, M. P. Shabanov, V. I. Putlayev, Ya. Yu. Filippov, Y. D. Tretyakov, and V. K. Ivanov, Mat–wiss u Werkstofftech **39**, 822 (2008).
40. M. J. Moorcroft, J. Davis, and R. G. Compton, Talanta **54**, 785 (2001).
41. R. Astala and M. J. Stott, Chem. Mat. **17**, 4125 (2005).
42. S. V. Dorozhkin, Acta Biomaterialia **6**, 715 (2010).
43. G. Hermann, A. Trenin, R. Matz, M. Gafurov, A. Kh. Gilmutdinov, K. Yu. Nagulin, W. Frech, E. Bjorn, I. Grinshtein, and L. Vasilieva, Spec. Acta B: Atomic Spectroscopy **59**, 737 (2004).
44. M. Markovic, B. O. Fowler, and M. S. Tung, J. Res. Natl. Inst. Stand. Technol. **109**, 553 (2004).